A 6.78MHz Mid-Range Wireless Power Charging System for Milliwatt-Power-Level Long-term Biomedical Sensing Applications

Zhiqiang Xu and Esther Rodriguez-Villegas
Wearable Technologies Lab, Dept. Electrical and Electronic Engineering, Imperial College London, SW7 2AZ, UK
{zhiqiang.xu18, e.rodriguez}@imperial.ac.uk

***Abstract*—This paper presents a methodology and system architecture to supply power over mid-distance, in the context of bio-sensors for long-term vital monitoring purposes. The first part of the paper introduces a novel non-coupling coil array system with a beamforming-control algorithm to enhance the power transfer efficiency, up to 25cm distance, regardless of the receiver's position. In the second part an on-chip wireless power charger system with high efficiency and trimming function to charge the mAh-level NiMH battery and provide stabilized power supply to devices, is presented. Overall, the system achieves 0.74% power efficiency at a distance of up to 25cm (with 0.86% from the beamforming-control power transfer system and 86% from the wireless power charger system).**

***Index Terms*—wireless power transfer (WPT), non-coupling coil, beamforming-controlled power transfer (BCPT), system-on-chip (SOC), nickel–metal hydride (NiMH) battery charger**

I. Introduction

Eliminating the need to charge miniature biomedical devices has been an active area of research for more than 20 years. But the constraints of what can be achieved in terms of power delivery limit the devices specifications in all aspects, from physical size to system performance. Conventional approaches to providing sufficient and stabilized power supply includes: (a) wired charging; (b) wireless power transfer (WPT); (c) human body energy harvesting. However, they all have significant physical limitations: wired charging requires taking off devices to connect them to charge; WPT requires precise alignment between coils, and the power transfer efficiency (PTE) attenuates rapidly as the distance increases [1], [2]; whilst the PTE associated to human body energy harvesting is also low and difficult to improve because, amongst other things, human factors constraints [3]. Considering the trade-offs between the PTE and human factors/usability, WPT is possibly the optimum choice. However, even at short distances WPT systems suffer from the bottleneck of significant power efficiency loss when their coils positions and/or orientation change [4].

Recent research on WPT systems has shown that beamforming-controlled power transfer (BCPT) could solve the power efficiency loss problem caused by coil misalignment. BCPT systems measure the mutual coupling between receivers (RXs) and transmitters (TXs) and then tune TXs to deliver in-phased power waves to RXs to effectively enhance the PTE [5], [6]. However, there are two common issues in BCPT systems: (a) their TX coils need to be large size and have large spacing between each other to prevent critical PTE loss from coupling/crosstalk from TXs [7]; (b) the complexity of beamforming-control algorithms increases with the number of coils increases [8].

In addition, commercial biomedical devices in the context of long term sensing/monitoring are typically equipped with a rechargeable battery that stores and deliver the energy they need to operate. Lithium-anode based batteries are popular because of their high safety, low self-discharge rate, and high power density [10]. However, in a milliwatt-power-level application, they might not be the best choice when compared to Nickel-metal hydride (NiMH) batteries, which for the typical required capacity are smaller and lighter [11]. Moreover, the nominal voltage of a lithium-based battery needs to be charge is in excess of 3.7V, whereas a NiMH battery has a nominal voltage starting from 1.2V, resulting in higher efficiency for charging circuits. And in the context of a battery that can be charged daily via WPT, the main drawback of NiMH, namely its high self-discharge rate is not that important [12].

As a summary, this paper presents a novel system architecture to harvest energy up to 25cm distances for long-term biomedical sensing/monitoring applications. The architecture relies on a beamforming-controlled algorithm on the TX side and a high-efficiency system-on-chip (SOC) wireless power charger on the RX side to charge and store the power. The paper structure is as follows. Section II describes the overall idea of the system. In section III, a non-coupling coil array structure and a BCPT algorithm are are presented which improve on the work presented in [9], targeting reducing complexity and size, whilst eliminating crosstalk. Section IV illustrates the architecture and functionality of the fully integrated wireless power charger for a 2.4V NiMH battery. Section V presents experiments and simulation results of the whole system. Section VI concludes the paper.

II. System overview

The proposed system diagram is shown in Fig. 1. The idea is that, within the context of long term monitoring, the device could be automatically charged whilst the user is sleeping, free of any charge cables. Hence, experiments for this work were carried out using a 17cm high-density foam mattress.

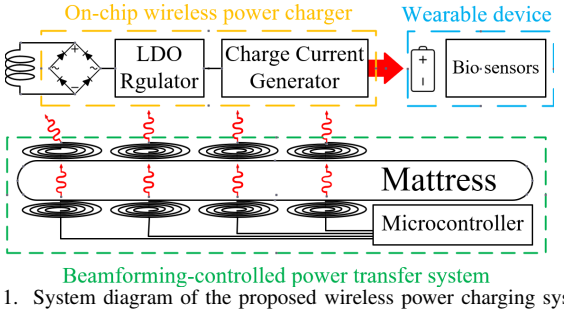

Fig. 1. System diagram of the proposed wireless power charging system.

This was justified on the basis that hospital-grade mattresses thickness is required to be over 12.5cm [13]. The wireless charging distance ranged from 17cm to 25cm from the TXs to the RX (which was 0cm to 8cm from the mattress to the RX). This took into account anthropometric characteristics, and the assumption the device would be placed on the user's arm [14]. This architecture operated at 6.78MHz following the Airfuel Alliance Standard for wireless charging and also because this is the lowest available frequency under the industrial, scientific and medical (ISM) band standard [15].

III. Beamforming-controlled power transfer system

A. Non-coupling coil structure

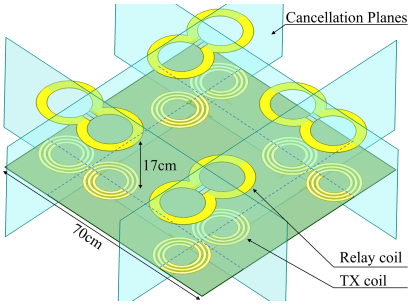

Fig. 2. Non-coupling coil structure.

Eight coils on the TX side were all designed as non-coupling dipole structures, in order to get better anti-crosstalk performance in a smaller area. The non-coupling structure consisted of two poles that generate two identical magnetic fields with opposite magnitude and combined into a zero-strength magnetic field area perpendicular to the centre. The next non-coupling coil placed in this zero-strength area could eliminate the crosstalk interference with the previous non-coupling coil. Hence, as shown in Fig. 2, the TX coil array consisted of four non-coupling coils, and each of them could minimise the crosstalk with adjacent coils. Furthermore, to overcome the power transfer loss over the 17cm mattress, a relay coil was added to each TX to enhance the power delivery. Four relay coils are also designed as non-coupling dipole structures to cancel the crosstalk interference. Each TX and its corresponding relay coil form an independent channel and could be treated as one unit. This greatly reduced the beamforming-control complexity, as explained below.

B. Beamforming control algorithm

The beamforming control algorithm proposed is based on magnetic coupling (mutual coupling) between TXs and a RX. This is the key to estimate the optimum way to tune the amplitude and phase of each TX. Once the transmitted power wave from the TX and relay array are finally in-phase, their electromagnetic waves are summed to maximise the PTE at the RX side. The magnetic coupling is derived by measuring the impedance difference when the RX is coupling with the coils on the TX side. In a conventional BCPT system, all the TX and relay coils on the TX side need to be detected to be able to derive the corresponding coupling, which results in complex architectures [16]. In a non-coupling structure, the magnetic couplings M_{TX} (between the TX and the RX) and M_{Relay} (between the relay and the RX) can be approximated to M_{TxR}, which is the magnetic coupling between the TX-relay link and the RX. Thus, the complexity is greatly reduced since the measurement only takes place in four TXs. Equation (1) and (2) shows the relationship between a TX-relay link and a RX.

$$V_{TxR} = I_{TxR}Z_{TxR} - j\omega M_{TxR}I_L \tag{1}$$

$$I_L(Z_R + R_L) = j\omega M_{TxR}I_{TxR} \tag{2}$$

where V_{TxR}, I_{TxR} and Z_{TxR} represent the voltage, current and impedance of the TX-Relay link. I_L, Z_R and R_L represent the load current, the impedance of the RX and the load resistance, respectively.

Meanwhile, the TX-relay's impedance is changed as a function of the coupling from the RX, and it can be directly calculated from $Z'_{TxR} = V_{TxR}/I_{TxR}$. By taking Z'_{TxR} into (1) and (2), rearranging the equation and substituting I_{TxR}, I_L, the magnetic coupling between the TX-relay link and the RX is derived as in (3).

$$\omega^2 M_{TxR}^2 = \left(Z'_{TxR} - Z_{TxR}\right)(Z_L + R_L) \tag{3}$$

The magnetic coupling between the RX and the other three TX-relay links can be found in the same way. Hence, the final beamforming-controlled voltage of each TX, V_{TxRi} is

$$V_{TxRi} = \beta(M_i Z_{TxRi} + \frac{M_i(M_1^2\omega^2 + M_2^2\omega^2 + M_3^2\omega^2 + M_4^2\omega^2)}{Z_R + R_L}) \tag{4}$$

where ω is the angular frequency (6.78MHz), Mi is short for M_{TxRi}, the magnetic coupling between TX-relay links and the RX, and β is the constant real value in relation to initial TX-relay parameters (I_{TxR}, Z_{TxR}) and can be derived under the initial TX equivalent input conditions. This is explained in details in [5].

C. PCB implementation and beamforming sensing

Four non-coupling TXs and four relay coils were fabricated on PCBs with 10oz and 1oz of copper thickness to achieve a high-quality factor of 445 and 380, respectively. All the TXs and relays were within a radius of 75mm. The receiver was a printed spiral coil with a radius of 20mm and a quality factor of 152. They were all designed taking into account safety considerations of human exposure to electromagnetic fields to prevent heat damage [17], whose specific absorption rate needs to be lower than 1.6W/Kg in any case.

As shown in Fig. 3, the prototype in the PCB contained four blocks: power amplifiers, gain/phase detectors, a radio frequency (RF) signal generator and a microcontroller. An

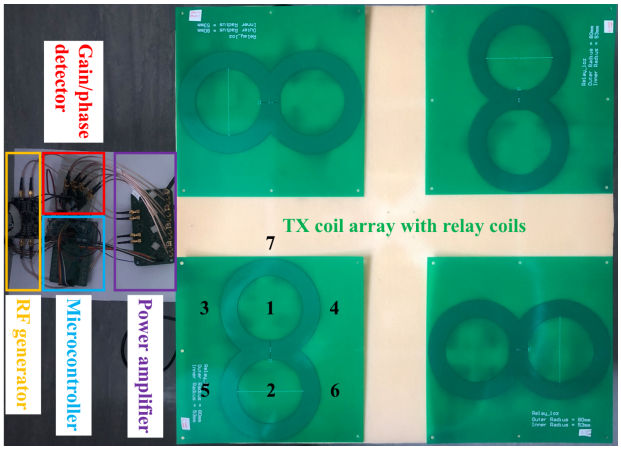

Fig. 3. Experiment setup (Numbers represents different receiver positions).

Arduino Due was used as a microcontroller to process the BCPT algorithm. The difference in impedance of the TX-relay link caused because of the existence of the RX was detected by using the gain/phase detector and the envelope detector circuits on the PCB. By sensing the gain/phase difference between the voltage of the power amplifiers and TXs, and their voltage amplitude, the magnetic coupling could be estimated and also the beamforming input.

IV. Circuit Implementation of Wireless Power Charger

A. System implementation

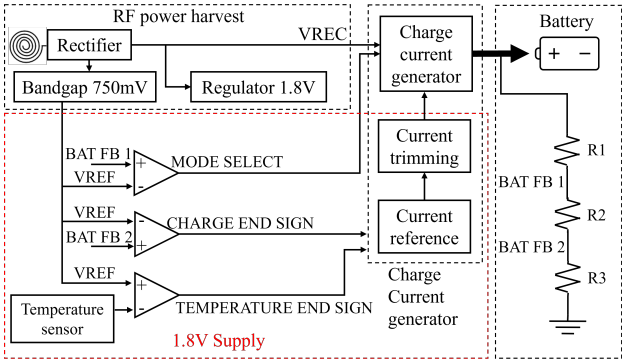

Fig. 4. System implementation of wireless power charger.

The integrated circuit part of the system was designed using TSMC 180nm BCD (Bipolar-CMOS-DMOS) technology. As shown in Fig. 4, it contains two parts, the power harvest module and the charger current generator. A rechargeable 2.4V 15mAh NiMH battery [18] would be placed off-chip. The system used a four-stage constant-voltage method to charge the battery [19]: (a) Soft-start stage at 450μA when the battery voltage is below the 2.4V ; (b) Accelerate charge stage at 3mA when the battery level is over 2.4V; (c) Trickle charge stage at 400μA for overnight protection when the battery level is near fully charged (approaches 2.9V at 20°C); (d) Thermal shutdown stage once the internal temperature rises over 45°C. Different charge stages are determined using strong-armed comparators [20] comparing the voltage of the feedback resistors R1, R2 and R3 with the bandgap voltage.

In order to achieve a high-efficiency wireless power charger system, it is necessary to achieve a high power conversion efficiency from the RF signal to a DC signal, and an RF limiter is required to prevent high voltages from damaging the chip. The current charger module included a current trimming function to overcome process corner variations, providing a solution to meet the charging standard of 2.4V for NiMH batteries with different capacities. Details about the different blocks are shown below.

B. RF power harvest module

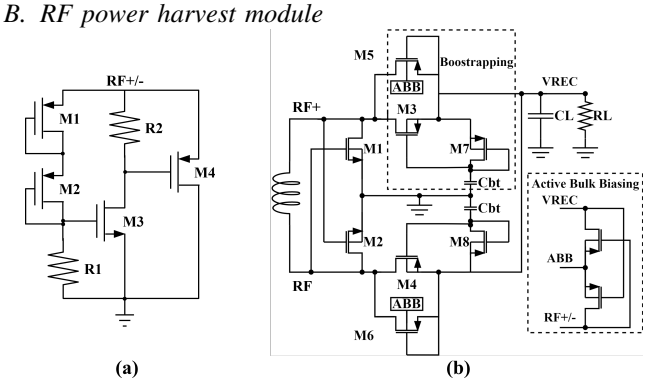

Fig. 5. (a) Passive RF limiter, (b) Full-wave rectifier with bootstrap and active bulk biasing technology [21].

1) RF limiter: To prevent excessive power delivered to the RX, which could damage the chip, a passive RF limiter is necessary to drain the redundant power into the ground. As shown in Fig. 5(a), two diode-connected transistors M1, M2 sense the RF input voltage level. And once this is over the threshold voltage, transistor M3 is turned on to pull the gate of the large-sized transistor M5 down to zero enabling all the redundant current to flow to the ground via M5. In this work, the circuit limited the inputs to 4.5V and worked with RF inputs from normal to 20V.

2) Full-wave rectifier with active bulk biasing technology: Conventional rectifiers using diode-bridged and cross-coupled structures suffer from low power efficiency (around 70%) and output voltage drop due to charge leakage from not-fully-off PMOS transistors [22]. Hence, the rectifier in Fig. 5(b) used a bootstrapping structure to eliminate the leakage problem. With the additional bootstrapping capacitor C_{bt}, the threshold voltage of M3/4 was reduced and hence the voltage drop is reduced. Also, active bulk biasing circuits [22] were used to keep the bulk of PMOS transistors at the highest potential from RF+/- and VREC to prevent current flow into the bulk.

The used rectifier with a 1KΩ load achieved 89.3% of power efficiency and 90% of voltage efficiency.

C. Compensated current charger

1) Current trimming circuit: The current trimming function was implemented using current mirror structure. As shown in Fig. 6(a), current addition and subtraction are adjusted by pin P1-P4 and S1-S4 with width/length (W/L) ratio of 2:1, 4:1, 8:1, 16:1, respectively. With pins P_EN and S_EN activating the trimming function, the generated fast mode charge current can be trimmed from 1.5mA to 4.8mA at steps of 0.1mA, controlled by pins P1-P4 and S1-S4.

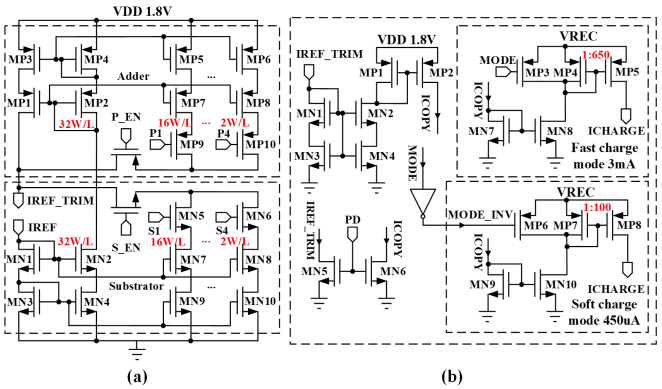

Fig. 6. Schematics of (a) Current trimming circuit, (b) Charge current generator with mode switching function.

2) Charge current generator: This circuit generated the three different current charging (ICHARGE) modes, for the battery, as shown in Fig. 6(b). Soft-start mode and fast mode can be switched via pin MODE. ICHARGE was obtained by using a 1:100 MP7:MP8, and 1:650 MP4:MP5 scaling respectively. Transistors MN5 and MN6 had a small W/L ratio to partly pull down the fast mode current to maintain the trickle mode current when the battery level is approaching full.

V. Testing Results

TABLE I

PTE between equivalent inputs and beamforming inputs versus position (aligned/misaligned)

Position	Equivalent input power/efficiency	Beamforming input power/efficiency
1 (20cm aligned)	39.2mW (2.45%)	105.8mW (6.62%)
2 (20cm aligned)	32.3mW (2.02%)	88.2mW (5.52%)
3 (20cm misaligned)	5.6mW (0.35%)	17.3mW (1.08%)
4 (20cm misaligned)	5.8mW (0.36%)	18.1mW (1.13%)
5 (20cm misaligned)	5mW (0.31%)	17.3mW (1.08%)
6 (20cm misaligned)	3.7mW (0.23%)	16.2mW (1.01%)
7 (20cm misaligned)	7.2mW (0.45%)	20mW (1.25%)
1 (25cm aligned)	4.8mW (0.3%)	13.8mW (0.86%)
2 (25cm aligned)	4mW (0.25%)	12.5mW (0.78%)

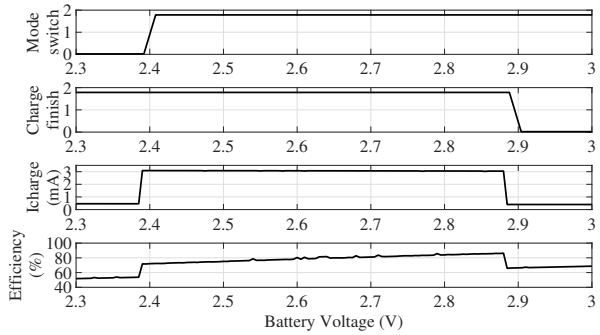

Fig. 7. Battery voltage versus charge mode switch sign, charge finish sign, charge current and charge efficiency (top to bottom).

In the test stage, we used a receiver coil with 50Ω load as the wearable devices at different heights and positions. The total TX input power was set as 1.6W, and the results were directly probed by an oscilloscope Agilent 3054A. As shown in Table I, the results for comparison were measured with the maximum amplitude in all the TX inputs, and only their phase is tuned after computing the beamforming algorithm. The results shown are the median from several experiments with different positions (the position number shown in Fig. 3) over 20cm. It can be seen how the power efficiency significantly improved with the beamforming inputs. The receiver harvests over 100mW power while aligned, and it can still get over 16mW power while misaligned. Furthermore, at 25cm the receiver can get 13.8mW, which is enough to charge a 2.4V 15mAh NiMH battery with a fast mode 3mA charge current.

Fig. 7 shows the simulation results of the wireless power charger at 20°C, with the battery level increasing from 2.3V to 2.9V, without enabling the current trimming function. The charge efficiency figure at the bottom is the power fed into the battery divided by the system's total power consumption (without the rectifier and RF limiter part). It can be seen how this reached 86% with the battery level increasing. Hence, considering the receiver is placed at a position such that the internal RF limiter is at quiescent mode, the RX-to-battery efficiency is 86%.

VI. Conclusion

TABLE II

Performance comparison

	[23]	[8]	[24]	This work
BCPT Method	Passive	Active	WPT	Passive
Frequency f	1MHz	6.78MHz	6.78MHz	6.78MHz
Distance D	40cm	20cm	14cm	up to 25cm
Radius of RX coil	40mm	80mm	200mm	20mm
Radius of TX/relay coil	125mm × 6	100mm × 5	400mm rectangular	75mm × 8
TX-to-RX efficiency η	11%	16%	70%	6.62% at 20cm 0.86% at 25cm
FOM (10^6)	0.52	0.44	0.45	1.34 at 20cm 0.04 at 25cm

This paper investigated the feasibility of a mid-range wireless power charging system for long-term biomedical sensing/monitoring wearable devices. A prototype was built to demonstrate the concept, assuming a wearable with a 2.4V 15mAh battery that would need to be recharged wirelessly whilst the patient is sleeping. A beamforming-control algorithm was used to optimise the power delivery. A 0.87% TX-to-RX efficiency was achieved in the coil at a distance of 25cm, which together with the proposed on-chip wireless charging system for small 2.4V NiMH batteries, satisfies the demands for most biomedical wearable sensors [25].

Table II shows key specifications of this work in comparison to the state-of-art designs for mid-range power charging applications. A figure of merit is defined to better establish a comparison within the context of this particular application, given by:

$$FOM = (f \cdot \eta^2 \cdot D^3)/(A_{TX} \cdot A_{RX}) \quad (5)$$

where A_{TX} and A_{RX} are the area of transmitter and receiver coils, respectively. D is the distance between the coils (according to the near-field electromagnetic theory, the magnetic field strength of multipole sources attenuate by the inverse cube of the distance [26]), η is the achieved transmitter to receiver efficiency (obeys square law with coils' coupling coefficient [27]) and f is the frequency of transmission (frequency is in a linear relationship with signal attenuation [28]).

As shown in Table II, at 20cm, the architecture presented in this work achieved a much better FOM than others, thanks to the benefits of the non-coupling structure and beamforming

control algorithm. However, due to the receiver's size and safety limits constraints, the quality factor was less. This led to its decreased FOM at 25cm, which is something that will need to be further investigated and improved upon in the future, if the distance in the real-life application requires it.

ACKNOWLEDGMENT

This work was supported in part by the European Research Council under Grant 724334.

REFERENCES

[1] X. Wei, Z. Wang, and H. Dai, "A Critical Review of Wireless Power Transfer via Strongly Coupled Magnetic Resonances," Energies, vol. 7, no. 7, 2014.

[2] A. M. Jawad, R. Nordin, S. K. Gharghan, H. M. Jawad, and M. Ismail, "Opportunities and Challenges for Near-Field Wireless Power Transfer: A Review," Energies, vol. 10, no. 7, 2017.

[3] Y. Zou, L. Bo, and Z. Li, "Recent progress in human body energy harvesting for smart bioelectronic system," Fundamental Research, vol. 1, no. 3, pp. 364-382, 2021.

[4] J. P. K. Sampath, A. Alphones, and D. M. Vilathgamuwa, "Coil optimization against misalignment for wireless power transfer," in 2016 IEEE 2nd Annual Southern Power Electronics Conference (SPEC), 5-8 Dec. 2016 2016, pp. 1-5.

[5] L. Shi, Z. Kabelac, D. Katabi, and D. Perreault, "Wireless Power Hotspot that Charges All of Your Devices," presented at the Proceedings of the 21st Annual International Conference on Mobile Computing and Networking, Paris, France, 2015.

[6] Z. Li and Z. Sun, "Enabling Magnetic Beamforming in MIMO Wireless Power Transfer Using Reconfigurable Metasurface," in GLOBECOM 2020 - 2020 IEEE Global Communications Conference, 7-11 Dec. 2020 2020, pp. 1-6.

[7] K. Hamano, K. Ohtsuka, R. Tanaka, and K. Nishikawa, "4×1 Multi-input single-output magnetic resonance beamforming wireless power transfer system," in 2017 International Applied Computational Electromagnetics Society Symposium (ACES), 1-4 Aug. 2017 2017, pp. 1-2.

[8] Y. Zhao, X. Li, Y. Ji, and C. Xu, "Random Energy Beamforming for Magnetic MIMO Wireless Power Transfer System," IEEE Internet of Things Journal, vol. 7, no. 3, pp. 1773-1787, 2020.

[9] H. Kim, K. Kim, S. Han, D. Seo, and J. Choi, "Nearly Non-Coupling Coil Array Allowing Many Independent Channels for Magnetic Communication," IEEE Access, vol. 6, pp. 34190-34197, 2018.

[10] Bock, David C et al. "Batteries used to Power Implantable Biomedical Devices." Electrochimica acta vol. 84 (2012): 10.1016/j.electacta.2012.03.057.

[11] A. Fayeez, V. Gannapathy, I. S. Isa, M. Nor, and N. L. Azyze, "Literature review of battery-powered and solar-powered wireless sensor node," vol. 10, pp. 671-677, 01/01 2015.

[12] Y. Liang et al., "A review of rechargeable batteries for portable electronic devices," InfoMat, https://doi.org/10.1002/inf2.12000 vol. 1, no. 1, pp. 6-32, 2019/03/01 2019.

[13] IEC 60601-2-52:2009, "Medical electrical equipment — Part 2-52: Particular requirements for the basic safety and essential performance of medical beds."

[14] D. Gupta, "2 - Anthropometry and the design and production of apparel: an overview," in Anthropometry, Apparel Sizing and Design, D. Gupta and N. Zakaria Eds.: Woodhead Publishing, 2014, pp. 34-66.

[15] "Wireless Power Transfer. AirFuel Resonant Baseline System Specification (BSS)," Wireless Power Transfer. AirFuel Resonant Baseline System Specification (BSS), pp. 1-100, 2017.

[16] B. Ma, Y. Zhao, X. Li, Y. Ji, and C.-Z. Xu, "Magnetic Beamforming Algorithm for Hybrid Relay and MIMO Wireless Power Transfer," Cham, 2019: Springer International Publishing, in Wireless Algorithms, Systems, and Applications, pp. 225-234.

[17] "IEEE Standard for Safety Levels with Respect to Human Exposure to Radio Frequency Electromagnetic Fields, 3 kHz to 300 GHz," IEEE Std C95.1, 1999 Edition, pp. 1-83, 1999.

[18] VARTA Microbattery GmbH. "V 15 H Rechargeable NiMH Button Data Sheet."

[19] Energizer Brands, LLC. "Nickel Metal Hydride (NiMH) Handbook and Application Manual."

[20] B. Razavi, "The StrongARM Latch [A Circuit for All Seasons]," IEEE Solid-State Circuits Magazine, vol. 7, no. 2, pp. 12-17, 2015, doi: 10.1109/MSSC.2015.2418155.

[21] S. S. Hashemi, M. Sawan, and Y. Savaria, "A High-Efficiency Low-Voltage CMOS Rectifier for Harvesting Energy in Implantable Devices," IEEE Transactions on Biomedical Circuits and Systems, vol. 6, no. 4, pp. 326-335, 2012.

[22] S. T. Kim, T. Song, J. Choi, F. Bien, K. Lim, and J. Laskar, "Semi-active high-efficient CMOS rectifier for wireless power transmission," in 2010 IEEE Radio Frequency Integrated Circuits Symposium, 23-25 May 2010 2010, pp. 97-100.

[23] J. Jadidian and D. Katabi, "Magnetic MIMO: how to charge your phone in your pocket," presented at the Proceedings of the 20th annual international conference on Mobile computing and networking, Maui, Hawaii, USA, 2014.

[24] L. Lan, C. H. Kwan, J. M. Arteaga, D. C. Yates, and P. D. Mitcheson, "A 100W 6.78MHz Inductive Power Transfer System for Drones," in 2020 14th European Conference on Antennas and Propagation (EuCAP), 15-20 March 2020 2020, pp. 1-4.

[25] G. Rong, Y. Zheng, and M. Sawan, "Energy Solutions for Wearable Sensors: A Review," Sensors, vol. 21, no. 11, 2021.

[26] Stratton, Julius Adams. Electromagnetic Theory. Hoboken, New Jersey: John Wiley & Sons, Inc., 2015.

[27] D. Ahn and M. Ghovanloo, "Optimal Design of Wireless Power Transmission Links for Millimeter-Sized Biomedical Implants," IEEE Transactions on Biomedical Circuits and Systems, vol. 10, no. 1, pp. 125-137, 2016.

[28] M. Mischi, N. G. Rognin, and M. A. Averkiou, "2.15 - Ultrasound Imaging Modalities," in Comprehensive Biomedical Physics, A. Brahme Ed. Oxford: Elsevier, 2014, pp. 361-385.